

A New Structure Type of the Ternary Sulfide $\text{Eu}_{1.3}\text{Nb}_{1.9}\text{S}_5$

N. R. Khasanova,¹ G. Van Tendeloo, O. I. Lebedev, and S. Amelinckx

EMAT, University of Antwerp (RUCA), Groenenborgerlaan 171, B-2020, Antwerp, Belgium

and

A. Yu. Grippa, A. M. Abakumov, S. Ya. Istomin, O. G. D'yachenko, and E. V. Antipov

Department of Chemistry, Moscow State University, Moscow 119899, Russia

Received August 22, 2001; in revised form December 18, 2001; accepted January 4, 2002

The structure model for the $\text{Eu}_{1.3}\text{Nb}_{1.9}\text{S}_5$ compound is determined based on high-resolution electron microscopy evidence. This compound crystallizes in a hexagonal unit cell with $a = 8.8732(8)$ Å and $c = 23.45(1)$ Å. Its structure is built up as an alternating sequence of trigonal-prismatic NbS_2 layers of formula $[\text{Nb}_7\text{S}_{14}]$ and $[\text{Nb}(\text{Eu}_3\text{S}_4)_2]$ slabs along the c -direction. In the $[\text{Nb}(\text{Eu}_3\text{S}_4)_2]$ block the stacking of two close-packed (Eu_3S_4) layers creates octahedral interstices formed by S atoms; these cavities are occupied by Nb cations. The model is compared with structures of other Eu-containing niobium sulfides, such as $\text{Eu}_{0.167}\text{NbS}_2$ and the misfit compound $(\text{EuS})_{1.5}[\text{NbS}_2]_{1.15}$. © 2002 Elsevier Science (USA)

INTRODUCTION

Layered transition-metal dichalcogenides TX_2 have attracted special attention because of their structural chemistry and peculiar electronic properties (superconductivity, charge-density-wave formation). A three-layer slab (TX_2) of a transition-metal layer (T) sandwiched between two close-packed chalcogenide layers (X_2) forms the basic building block. The coordination of the metal atoms can be either octahedral or trigonal-prismatic. The bonding within the slabs is much stronger than the interaction between them. A variety of guest species can be accommodated into this interlayer gap without disturbing the TX_2 layers; formally they can be considered “intercalated compounds.” Depending on the inserted atoms and the degree of “intercalation,” the derivatives obtained can adopt different types of structures.

¹To whom correspondence should be addressed. Fax: +007-9394788. E-mail: nellie@icr.chem.msu.ru.

In $M_x\text{NbS}_2$ compounds ($M = \text{alkali metal, Ag, Pb, Sn, Bi}$) small cations M^{n+} are ordered in the octahedral interstices between NbS_2 slabs, while for large M^{n+} , trigonal-prismatic cavities are preferable (1). The structure of the misfit compounds $(MS)_{1+x}(\text{NbS}_2)_m$ ($M = \text{Pb, Sn, Bi, rare earth elements, } m = 1-3 \text{ and } x \approx 0.1$) can be described as an alternating stacking of NbS_2 sandwiches and MS layers with a distorted rock-salt structure. These two slabs with a strong intralayer bonding are incommensurate, and the interaction between them leads to a mutual modulation with the wave vector for one system being dictated by the other subsystem (2).

Compounds of empirical formula “ $A\text{Nb}_2\text{S}_5$ ” were also obtained with alkaline earth elements ($A = \text{Ba, Sr}$). Though the composition of the “ $A\text{Nb}_2\text{S}_5$ ” is very similar to that of the misfit bilayer compounds $(MS)_{1+x}(\text{NbS}_2)_2$, they appear to be structurally different. According to X-ray diffraction they crystallize in a hexagonal unit cell. A strong effect of preferential orientation reflects the layered character of the structure. Electron diffraction, on the other hand, reveals the presence of complex superstructures in the ab -plane. These ternary sulfides exhibit different physical properties (metallic for BaNb_2S_5 , superconducting for SrNb_2S_5), and the diversity of the transport properties even increases with the Ta and V analogs. However, little structural information about these compounds is available due to the lack of single-crystal data and to the complexity of the structures (3–5).

The recently prepared “ EuNb_2S_5 ” compound can be considered as the Eu-containing analogue of this “ $A\text{T}_2\text{S}_5$ ” family ($A = \text{Sr, Ba}$ and $T = \text{Nb, Ta}$). Similar to the SrNb_2S_5 compound it has a $\sqrt{7}a \times \sqrt{7}a$ superstructure and exhibits a superconducting transition at 3 K (6). Because of problems in preparing single crystals and the difficulties in using X-ray powder diffraction, we attempted to solve

its structure by high-resolution electron microscopy (HREM).

EXPERIMENTAL

The $\text{Eu}_{1.3}\text{Nb}_{1.9}\text{S}_5$ compound was prepared from a starting mixture of EuS, Nb (Roth, 99.9%), and S (99.99%) in the Eu/Nb/S ratio 1.3/1.9/5.0. This mixture was heated in evacuated and sealed silica tubes at 1070°C for 70 h. EuS was obtained from $\text{Eu}_2(\text{SO}_4)_3 \cdot 8\text{H}_2\text{O}$ by heating in a H_2S flow at 900°C for 50 h, with one intermediate regrinding.

The sample obtained was characterized by X-ray powder diffraction (XRD) produced in a focusing Guinier camera using $\text{CuK}\alpha_1$ radiation and Ge as an internal standard. X-ray powder diffraction data were collected on a STOE STADI/P powder diffractometer ($\text{CuK}\alpha_1$ radiation, curved Ge monochromator, transmission and reflection modes, scintillation counter). The experimental density was measured by the pycnometric technique with CCl_4 as a working liquid.

Electron diffraction (ED) and high-resolution electron microscopy studies were performed with a JEOL 4000EX instrument. A Philips CM 20 microscope with a LINK-2000 attachment was used for electron diffraction. For the EDX analysis, results were based on the Eu (L), Nb (K), and S (K) lines in the spectra. Specimens for electron microscopy were obtained by crushing in methanol and mounting the crystal fragments on a Cu grid covered with a carbon-coated holey film. Image simulations were carried out with a Mac Tempas software program, in which the following parameters were used: C_s : 1.0 mm, objective aperture: 9 nm^{-1} , beam convergence: 0.55 mrad, and mechanical vibration: 0.03 nm. The thickness as well as the defocus was varied.

RESULTS

According to the XRD analysis the prepared sample was found to be single phase, with a measured density of $4.8(1)\text{ g/sm}^3$. The most intense reflections on the XRD pattern were indexed on a hexagonal unit cell of $a = 3.353(1)\text{ \AA}$ and $c = 23.45(1)\text{ \AA}$, with the reflection condition: $000l, l = 2n$. An ED study, however, revealed the presence of a $\sqrt{7}a \times \sqrt{7}a$ superstructure in the $[0001]^*$ zone; therefore, a complete indexing of the XRD pattern, including the low-intensity reflections, was done in a hexagonal unit cell with $a_{\text{sup}} = 8.8732(8)\text{ \AA}$ and $c_{\text{sup}} = 23.45(1)\text{ \AA}$. The XRD observation in reflection and transmission modes also revealed a strong effect of preferred orientation reflecting the layered character of the material. Since the average separation between S layers in NbS_2 and its derivatives is about 2.9–3.2 \AA , one can assume a stacking of 8 S-based slabs in the repeat unit along the c direction.

The composition, as determined by EDX, was found to be $\text{Eu:Nb:S} = 16.2(7):23(1):61(1)$, which corresponds to the chemical formula $\text{Eu}_{1.3(1)}\text{Nb}_{1.9(1)}\text{S}_{5.0(1)}$ and agrees well with the initial composition. We particularly paid attention to the possible presence of oxygen in the compound; however, no oxygen peak was detected in the EDX spectrum.

ED patterns of the most relevant zones are presented in Fig. 1. The brighter reflections in the $[0001]^*$ ED pattern can be indexed on the basis of a hexagonal subcell with $a \approx 3.3\text{ \AA}$, the weaker reflections indicate the presence of a $\sqrt{7}a \times \sqrt{7}a$ superstructure. Figure 2 shows the relation between the vectors of the superstructure unit cell ($\mathbf{A}_1, \mathbf{A}_2, \mathbf{A}_3$) and the vectors of the basic unit cell ($\mathbf{a}_1, \mathbf{a}_2, \mathbf{a}_3$) in real space, where $|\mathbf{A}_1| = |\mathbf{A}_2| = \sqrt{7}a$ and $|\mathbf{A}_3| = |\mathbf{a}_3| = c$. The relation is described by the following transformation matrix

$$\begin{pmatrix} \mathbf{A}_1 \\ \mathbf{A}_2 \\ \mathbf{A}_3 \end{pmatrix} = \begin{bmatrix} 3 & 1 & 0 \\ -1 & 2 & 0 \\ 0 & 0 & 1 \end{bmatrix} \begin{pmatrix} \mathbf{a}_1 \\ \mathbf{a}_2 \\ \mathbf{a}_3 \end{pmatrix}.$$

All ED patterns can be completely indexed with the c parameter of 23.5 \AA . Systematic absence of $000l, l \neq 2n$ reflections is observed on the $[1\bar{1}00]^*$ and $[1\bar{2}10]^*$ ED patterns, but in the $[5\bar{4}\bar{1}0]^*$ pattern weak $000l$ reflections with $l \neq 2n$ are present. These spots, however, disappear when the crystallite is tilted around the $[0001]^*$ axis and therefore they are attributed to double diffraction. This extinction rule is in agreement with the XRD data.

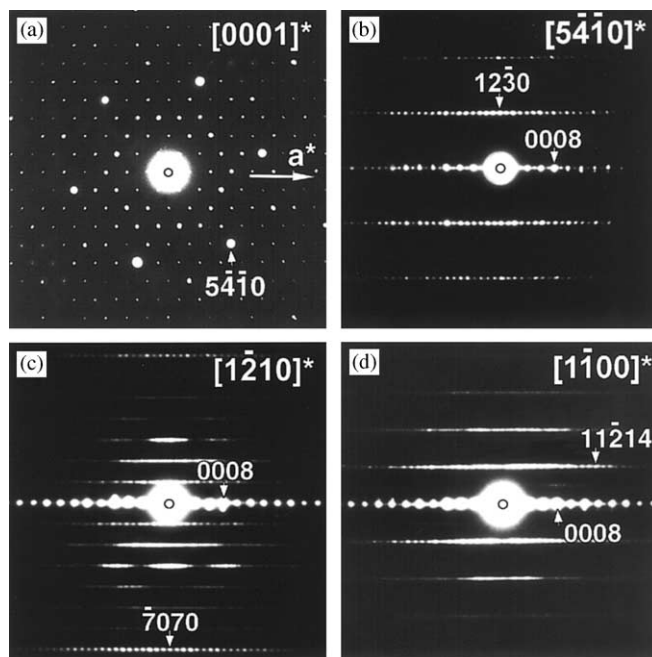


FIG. 1. Electron diffraction patterns along different zone axes for $\text{Eu}_{1.3}\text{Nb}_{1.9}\text{S}_5$.

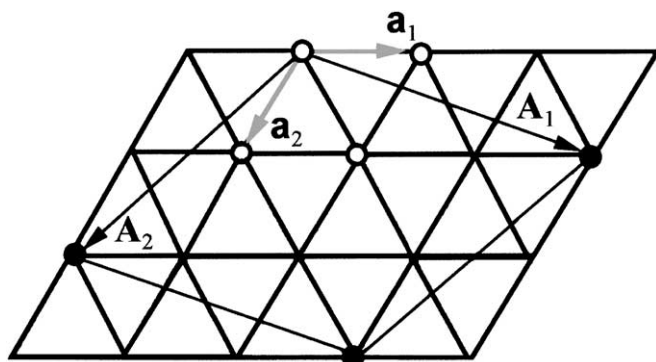


FIG. 2. Schematic representation of transformation from subcell to supercell in the direct space.

Considerable streaking is invariably observed along rows of superlattice reflections on the $[1\bar{2}10]^*$ and $[1\bar{1}00]^*$ ED patterns, while rows of sublattice spots are not streaked. This effect will be discussed further.

We tried to determine the structure from HREM evidence, taking into account the composition data from EDX, the structure symmetry determined by ED, and the crystal chemistry of the constituent atoms. Experimental HREM images were then compared with those calculated using different structural models. For the subcell construction HREM images along the $[5\bar{4}10]$ zone are most useful (Fig. 3). This direction coincides with the $[\bar{1}2\bar{1}0]$ zone of the hexagonal subcell ($[5\bar{4}10]_{\text{sup}} = [\bar{1}2\bar{1}0]_{\text{sub}}$). Simulated images indicate that under the given conditions of thickness (32 Å) and a defocus close to Scherzer defocus, atoms are imaged in black. Triangle-shaped, black “furrows” are associated with the NbS_2 slabs, assuming the Nb atoms to occupy the trigonal-prismatic cavities. Since superconductivity in niobium disulfide and its derivatives is most often observed

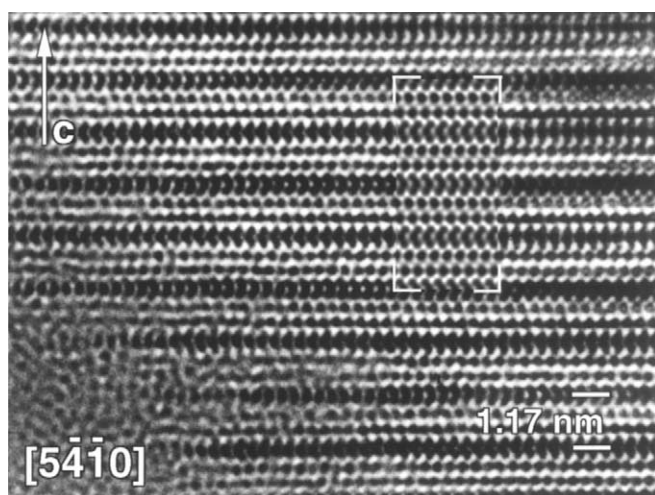


FIG. 3. Image view along the $[5\bar{4}10]$ axis that corresponds to subcell view along the close-packed direction. Inset: Image simulation obtained for a second model at defocus value $\Delta f = -350 \text{ \AA}$ and thickness $t = 32 \text{ \AA}$.

with trigonal-prismatic coordination of Nb atoms, this assumption is quite reasonable. The excellent fit between image and simulations allows the deduction of the stacking sequence along the c -axis $\dots AcABCBA BABAcA \dots$ described by the $P6_3$ space group. Capital and small letters, respectively, denote the sulfur layers and the niobium layers. The superlattice is geometrically constructed by applying the transformation matrix, which multiplies the number of atoms in each layer by 7. The proposed model is built up of eight S-based layers with an average interlayer S–S separation of 2.9 Å, and contains two Nb_7S_{14} slabs separated by double S_7 layers.

A number of layered transition-metal dichalcogenides are known to exhibit charge-density-wave (CDW) formation (i.e., in NbS_2 and TaS_2 (7)). To verify whether the superstructure is related to CDW, an *in situ* heating experiment was performed with the crystal oriented along $[0001]^*$. The superstructure, however, was found to be stable up to 760°C, without any significant change in the superstructure reflections. Such behavior on heating is not consistent with an idea of charge localization in the NbS_2 slabs as the origin of the superstructure. Since the observed superconductivity points toward the presence of undistorted trigonal-prismatic NbS_2 layers, it is reasonable to suggest that the superstructure appears due to ordering within other layers.

The obtained framework of eight S-based layers with Nb atoms in a trigonal-prismatic coordination corresponds to the composition $\text{Nb}_{14}\text{S}_{56}$. To be in agreement with the measured chemical composition additional Eu and Nb atoms should be incorporated into this supercell matrix. The following possibilities were considered and subsequently verified:

- Eu and additional Nb cations are placed into the interstices formed by the S-based layers;
- Eu and S atoms form mixed $(\text{Eu},\text{S})_7$ layers sandwiched by Nb_7S_{14} slabs.

The stacking sequence deduced above produces octahedral and tetrahedral interstices between the S-based layers; these interstices can be occupied by Eu or Nb. Insertion of 12 Eu and 6 Nb cations into octahedral cavities (more favorable from a crystal chemistry point of view) introduces a $\sqrt{7}a \times \sqrt{7}a$ superstructure and leads to the composition $\text{Eu}_{12}\text{Nb}_{20}\text{S}_{56}$, close to the measured one. However, the $[5\bar{4}10]$ HREM image calculated based on this model has a poor correspondence with the experimental image and therefore this model has to be rejected.

Next, a mixed occupation of the hexagonal layer by Eu and S atoms is considered. Each layer of the supercell consists of seven atoms, distributed over three independent positions. Due to the symmetry restrictions only one, three, four, six or seven Eu atoms can be located in this layer. Occupation of this mixed layer by one, four, or six Eu atoms, however, leads to stoichiometry problems, while a

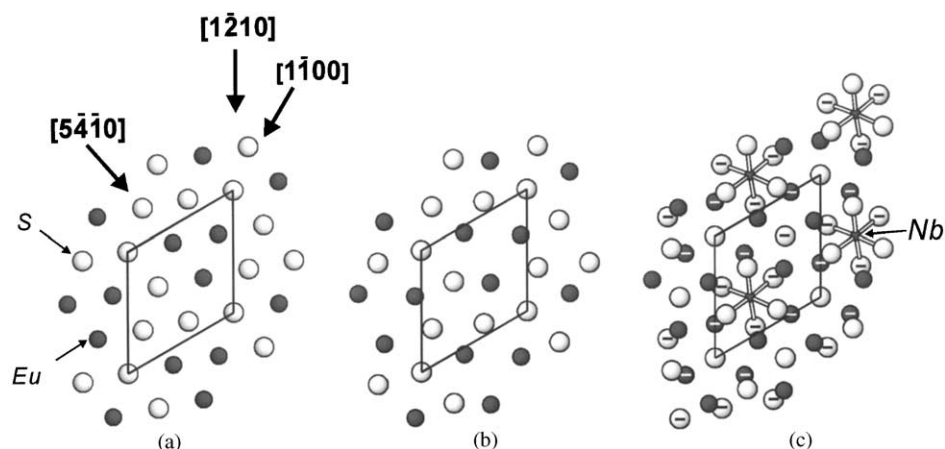


FIG. 4. [0001] projection of the (Eu_3S_4) layer: (a) Single layer with an ideal hexagonal arrangement which leads to short Eu–Eu interatomic distances. (b) Modified single layer with atoms shifted from their ideal positions to achieve a reasonable coordination. (c) Two successive (Eu_3S_4) layers; atoms at the lower level are marked with a minus sign. Nb atoms between these two (Eu_3S_4) layers (in octahedral coordination) are also shown. Directions are indicated in superstructure notation and the superstructure unit cell is outlined.

mixed layer with a (Eu_3S_4) composition satisfies the atomic ratios determined by EDX. $(\text{Sr}_3\text{S}_3\text{O})$ hexagonal layers have recently been observed in $\text{Sr}_6\text{V}_9\text{S}_{22}\text{O}_{22}$, which has a similar in-plane superstructure (8). Sr^{2+} and Eu^{2+} have a close ionic radius, and therefore the existence of mixed (Eu_3S_4) layers in Eu-containing niobium disulfide looks reasonable and is used as a trial model.

Within the ideal hexagonal (Eu_3S_4) layer Eu atoms form triangles with short Eu–Eu distances of 3.35 Å (Fig. 4a). To avoid close interaction and to obtain a reasonable coordination, Eu and S atoms were moved away from their ideal position; a modified (Eu_3S_4) layer is shown in Fig. 4(b, c). Atom shifts are also limited by the requirement

to maintain agreement with HREM images along different directions. Particularly the $[5410]$ HREM observation, imaging the subcell, is very sensitive to atom displacements.

Different stacking of two (Eu_3S_4) layers creates one octahedral or two tetrahedral interstices formed by the sulfur atoms from these layers. These cavities can be occupied by additional Nb cations, which is necessary for obeying the chemical composition. Two structure models can therefore be proposed: in the first model Nb cations occupy the two tetrahedral interstices, while in the second model one Nb atom is situated in the octahedral cavity (Figs. 5a, 5b). While octahedral coordination of Nb is often observed in NbS_2 derivatives, tetrahedral coordination of

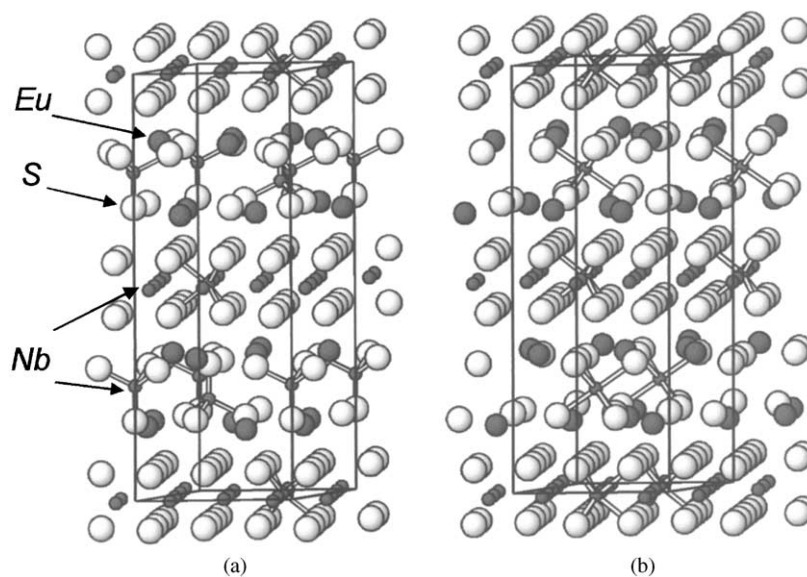


FIG. 5. Proposed structural models: the coordination of Nb atoms is represented as (a) trigonal prismatic and tetrahedral (first model) and (b) trigonal prismatic and octahedral (second model).

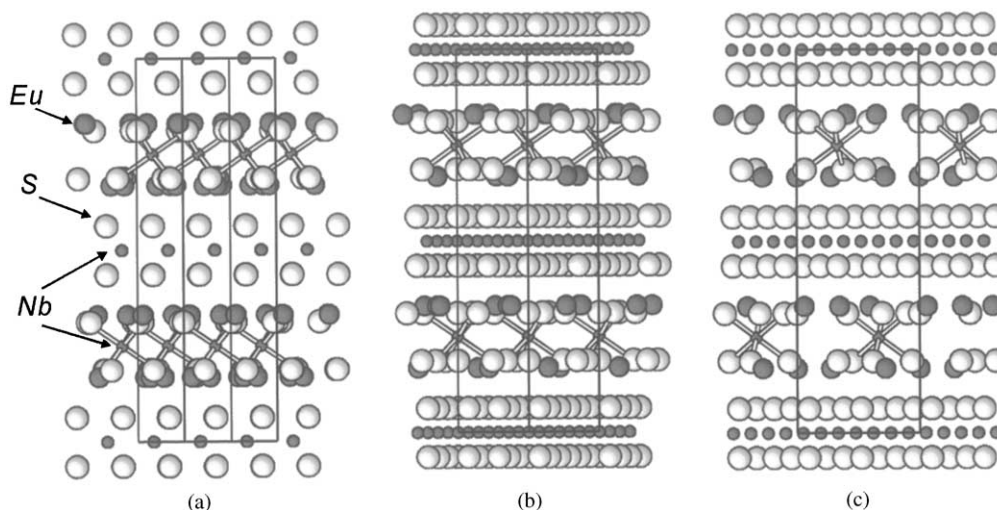


FIG. 6. Projections of the structure of $\text{Eu}_{1.3}\text{Nb}_{1.9}\text{S}_5$ (second model) along the (a) $[5\bar{4}10]$, (b) $[1\bar{1}00]$, and (c) $[1\bar{2}10]$ zone axes.

Nb is exceptional and usually related to Nb^{5+} (9). Such a high oxidation state is hard to be realized under the synthesis conditions used here. Therefore, the second model, with Nb in an octahedral coordination between two Eu_3S_4 slabs, is to be preferred from a crystal chemistry point of view. Nevertheless, for both models image simulations were made and compared with the experimental ones.

The $[5\bar{4}10]$, $[1\bar{1}00]$, and $[1\bar{2}10]$ HREM images were used for comparison between experiment and simulation. Only along the $[5\bar{4}10]$ projection individual atom columns are separated; for the other directions the relationship between structure and image is not straightforward. Analysis of these calculated images also shows a preference for the second model. Though both models produce quite similar pictures for most zones, the difference between the two models is maximized for the $[1\bar{2}10]$ HREM image taken under underfocus conditions. For these conditions the simulation results for both models will be shown. For the other zones the experimental images will only be compared with the simulations based on the model with an octahedral Nb coordination, which turns out to be the more favorable, both on the base of crystal chemistry and image simulation.

Projections of the structure with Nb in an octahedral coordination are shown in Fig. 6 along the $[5\bar{4}10]$, $[1\bar{1}00]$, and $[1\bar{2}10]$ zones. From a comparison of the $[1\bar{2}10]$ simulated image with the corresponding projection white lines on the picture are attributed to NbS_2 slabs, while white dots correspond to the cation ordering in the (Eu_3S_4) layers (Fig. 7). Along the $[10\bar{1}0]$ direction double bright spots are spaced by 7.7 \AA , which agrees with the supercell periodicity along this direction. A well-defined ordering of the double-dot arrangement along the c -direction is clearly absent; this stacking disorder explains the streaking along

c^* of the $hkil$ reflections on the $[1\bar{1}00]^*$ and $[1\bar{2}10]^*$ ED patterns. At the same time the periodicity is preserved along and across the NbS_2 slabs, causing well-defined sublattice spots on ED patterns. To simplify further image simulation a structural fragment with a c -parameter of $\sim 23.5 \text{ \AA}$ (Fig. 7) was chosen, and the simulated image was found to fit well the experimental observation.

For the $[5\bar{4}10]$ and $[1\bar{1}00]$ zones this model produces a good correspondence with the experimental images. The $[5\bar{4}10]$ image has already been discussed (Fig. 3). In the $[1\bar{1}00]$ zone atom columns within the Nb_7S_{14} slabs are not resolved and are projected as black continuous lines in the image (Fig. 8). Black zig-zags containing “furrows”

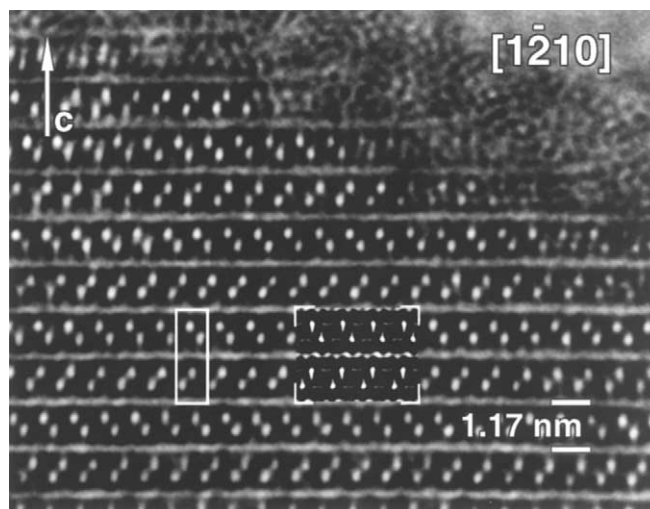


FIG. 7. High-resolution image of $\text{Eu}_{1.3}\text{Nb}_{1.9}\text{S}_5$ along the $[1\bar{2}10]$ axis under overfocus conditions. The unit cell chosen for structure modeling is outlined. Inset: Image simulation calculated for the final model with $\Delta f = 320 \text{ \AA}$, $t = 44 \text{ \AA}$.

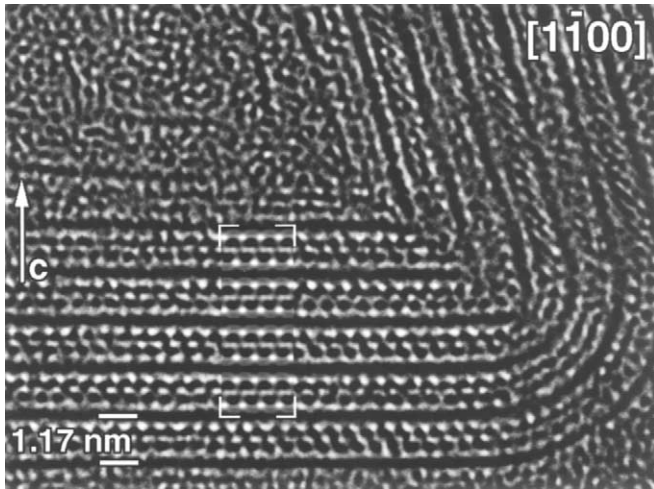


FIG. 8. High-resolution image view of $\text{Eu}_{1.3}\text{Nb}_{1.9}\text{S}_5$ along the $[1\bar{1}00]$ zone axis. The image simulation given as inset was calculated for the second model with $\Delta f = -540 \text{ \AA}$, $t = 36 \text{ \AA}$.

correspond to triangular groups of Eu atoms in two (Eu_3S_4) layers joined through Nb atoms (compare with the projection in Fig. 6b). The separation between the zig-zags of 4.4 \AA coincides well with the superstructure periodicity along the $[11\bar{2}0]$ direction. The $[1\bar{2}10]$ HREM reveals also the presence of bent or curved crystals in the structure of $\text{Eu}_{1.3}\text{Nb}_{1.9}\text{S}_5$, which resembles the behavior of graphitic carbon and of the layered $2H\text{-MX}_2$ type pure dichalcogenide structures (10). Similar to them $\text{Eu}_{1.3}\text{Nb}_{1.9}\text{S}_5$ is probably able to incorporate defects in the form of non-six-membered rings, resulting in the formation of positive curvatures of the lattice; no atomic scale model for this curvature has been presented though.

As already mentioned the difference between the two models is most striking in the $[1\bar{2}10]$ HREM image taken under underfocus conditions (Fig. 9). According to the image simulation atoms are projected as black dots in this picture. The black continuous lines correspond to the NbS_2 slabs, showing no superstructure ordering, while the black assembling inbetween corresponds to the ordering of the (Eu_3S_4) layers. The images calculated with both models are shown as insets in Fig. 9. The second model with Nb atoms in an octahedral coordination clearly produces a better correspondence with the experimental image. The chemical composition $\text{Eu}_{1.36}\text{Nb}_{1.8}\text{S}_5$ estimated from this model is consistent with the results of EDX analysis. Moreover, the value of the density calculated with this model is in reasonable agreement with the experimental one: 4.90 g/cm^3 and $4.8(1) \text{ g/cm}^3$, respectively. These results support the crystal chemistry consideration and make the second model preferential. The atomic coordinates for this model are given in Table 1.

Like many structures based on the stacking of close-packed layers this compound exhibits stacking disorder,

which not only makes X-ray structure determination difficult, but even seriously hampers the HREM study. The defect microstructure contains translational disorder as well as rotational disorder; this is expressed in the ED patterns as well as in the HREM images. Diffraction patterns along $[hk\cdot 0]$ zones exhibit diffuse streaks along the c axis through all c^* rows of superstructure spots (Fig. 1).

Application of the cluster theory (11,12) to interpret diffuse scattering allows an exact, albeit qualitative explanation of the geometry of diffuse scattering. We use the following notations. The superstructure unit cell is based on the vectors ($\mathbf{A}_1, \mathbf{A}_2, \mathbf{A}_3$), whereas the basevectors of the hexagonal unit cell of the “host” structure are given by ($\mathbf{a}_1, \mathbf{a}_2, \mathbf{a}_3$). We note that

$$\mathbf{A}_1 = 3\mathbf{a}_1 + \mathbf{a}_2, \quad \mathbf{A}_2 = -\mathbf{a}_1 + 2\mathbf{a}_2$$

where

$$|\mathbf{A}_3| = |\mathbf{a}_3| = c \quad \text{and} \quad |\mathbf{A}_1| = |\mathbf{A}_2| = \sqrt{7}a.$$

The inverse relations are

$$\mathbf{a}_1 = 1/7(2\mathbf{A}_1 - \mathbf{A}_2), \quad \mathbf{a}_2 = (1/7)(\mathbf{A}_1 + 3\mathbf{A}_2). \quad [1]$$

The unit cell of the reciprocal lattice is called ($\mathbf{B}_1, \mathbf{B}_2, \mathbf{B}_3$) with $\mathbf{B}_i \cdot \mathbf{A}_j = \delta_{ij}$; diffraction vectors are then $\mathbf{g} = h\mathbf{B}_1 + k\mathbf{B}_2 + l\mathbf{B}_3$.

In reciprocal space all intensity is confined to fine lines parallel to \mathbf{A}_3 . Some of these lines are continuous; others consist of discrete spots with a $|\mathbf{B}_3| = c^*$. All such lines pass through basic spot positions; they can be represented analytically by the pair of simultaneous equations,

$$\sin \pi h = 0 \quad \sin \pi k = 0,$$

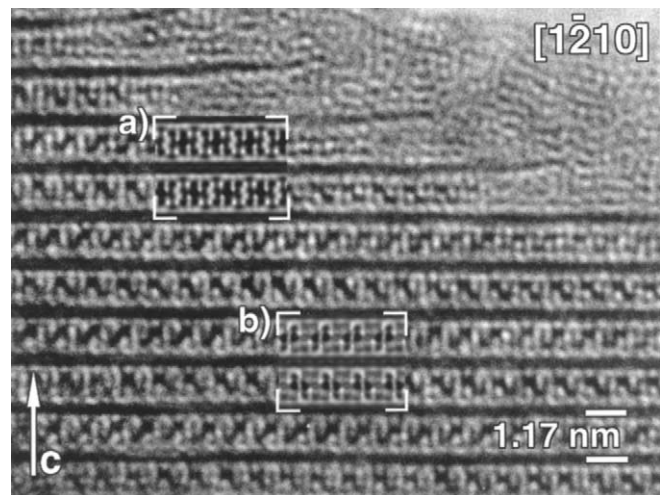


FIG. 9. The $[1\bar{2}10]$ HREM image of $\text{Eu}_{1.3}\text{Nb}_{1.9}\text{S}_5$ taken under underfocus conditions. Insets: Image simulations calculated for (a) first model with $\Delta f = -790 \text{ \AA}$, $t = 36 \text{ \AA}$, and (b) second model with $\Delta f = -760 \text{ \AA}$, $t = 48 \text{ \AA}$.

TABLE 1
Fractional Atomic Coordinates for $\text{Eu}_{1.3}\text{Nb}_{1.9}\text{S}_5$
Compound (Second Model)^a

Atom	Position	x	y	z
Eu1	6c	0.347	0.406	0.169
Eu2	6c	0.0	0.280	0.331
Nb1	2b	0.333	0.667	0.5
Nb2	6c	0.095	0.048	0.0
Nb3	6c	0.238	0.191	0.0
Nb4	2b	0.667	0.333	0.25
S1	6c	0.048	0.238	0.064
S2	6c	0.476	0.381	0.064
S3	2b	0.333	0.666	0.064
S4	2a	0.0	0.0	0.188
S5	6c	0.409	0.103	0.188
S6	2b	0.333	0.667	0.312
S7	6c	0.446	0.381	0.312
S8	2b	0.666	0.333	0.436
S9	6c	0.238	0.191	0.436
S10	6c	0.095	0.476	0.436

^aSpace group $P6_3$ (No. 173); $a_{\text{sup}} = 8.8732(8) \text{ \AA}$, $c_{\text{sup}} = 23.45(1) \text{ \AA}$; $Z = 1$ for the composition $\text{Eu}_{1.2}\text{Nb}_{1.6}\text{S}_{4.4}$.

when referred to the reciprocal supermesh ($\mathbf{B}_1, \mathbf{B}_2$) and considering h and k as continuous variables along \mathbf{B}_1 and \mathbf{B}_2 . In Fourier representation this become

$$e^{\pi i h} - e^{-\pi i h} = 0 \quad e^{\pi i k} - e^{-\pi i k} = 0. \quad [2]$$

Comparing these expressions with the general locus equation (11) $\sum_k \omega_k e^{2\pi i \mathbf{g} \cdot \mathbf{r}_k}$, where the \mathbf{r}_k are ‘‘cluster site vectors’’ one can rewrite Eq. [2] as

$$e^{2\pi i [hkl] \cdot \frac{1}{2}[100]} - e^{2\pi i [hkl] \cdot \frac{1}{2}[\bar{1}00]} = 0,$$

$$e^{2\pi i [hkl] \cdot \frac{1}{2}[010]} - e^{2\pi i [hkl] \cdot \frac{1}{2}[0\bar{1}0]} = 0,$$

where we have used the shorthand

$$[hkl] = h\mathbf{B}_1 + k\mathbf{B}_2 + l\mathbf{B}_3, \quad [3]$$

and

$$\frac{1}{2}[010] = \frac{1}{2}\mathbf{A}_2, \quad \frac{1}{2}[100] = \frac{1}{2}\mathbf{A}_1.$$

The ‘‘clustervectors’’ are thus $\pm \frac{1}{2}[010]$ and $\pm \frac{1}{2}[100]$ and $\omega_{100} = 1$, $\omega_{010} = -1$. The ‘‘clusterrelation’’ (11) $\sum_k \omega_k \bar{\sigma}_{k+j} = 0$ between the occupation parameters $\bar{\sigma}_k$ then reduces to

$$\bar{\sigma}_{\frac{1}{2}[100]} = \bar{\sigma}_{\frac{1}{2}[\bar{1}00]}, \quad \bar{\sigma}_{\frac{1}{2}[010]} = \bar{\sigma}_{\frac{1}{2}[0\bar{1}0]}.$$

These two relations have to be satisfied simultaneously. The geometrical interpretation is clearly that any motif located at $\frac{1}{2}[100]$ with respect to an arbitrary reference point of the lattice ($\mathbf{A}_1, \mathbf{A}_2$) must be the same as the motif at $\frac{1}{2}[\bar{1}00]$ with respect to the same reference point. In other

words, motifs separated by $[\bar{1}00]$ must be identical. The same applies to motifs separated by $[010]$.

In conclusion, in any (0001) lattice plane all motifs must be situated on a two-dimensional lattice built on the basevectors $\mathbf{A}_1 \equiv [100]$ and $\mathbf{A}_2 \equiv [010]$. There is no restriction concerning the third direction; i.e., the successive (0001) layers can be shifted over arbitrary displacement vectors \mathbf{R} . However the fact that not all c^* rows are continuous places restrictions on these displacements \mathbf{R} .

The condition for the occurrence of unstreaked reflections is $\mathbf{g} \cdot \mathbf{R} = \text{integer}$. We can limit our considerations to the basal plane since \mathbf{R} is perpendicular to $[0001]$; i.e., it is of the form $\mathbf{R} = m\mathbf{a}_1 + n\mathbf{a}_2$.

Taking Eqs. [1] and [3] into account we have

$$\mathbf{g} \cdot \mathbf{R} = [h\mathbf{B}_1 + k\mathbf{B}_2] \cdot [m\mathbf{a}_1 + n\mathbf{a}_2]$$

$$= \frac{1}{7}[h\mathbf{B}_1 + k\mathbf{B}_2] \cdot [m(2\mathbf{A}_1 - \mathbf{A}_2) + n(\mathbf{A}_1 + 3\mathbf{A}_2)].$$

That is,

$$\mathbf{g} \cdot \mathbf{R} = \frac{1}{7}[h(2m + n) + k(3n - m)].$$

We now take into account the experimental observation that the following lattice rows are discrete: $[12 \cdot l]$, $[70 \cdot l]$, $[31 \cdot l]$. This respectively leads to the condition $n = \text{integer}$, $2m + n = \text{integer}$, $m = \text{integer}$, and clearly means that only lattice vectors of the basal plane of the hexagonal host sublattice are permitted as displacement vectors. It strongly suggests that the disorder is associated with different positioning of the arrangement of Eu clusters within the S layers rather than with faults in the stacking of sulfur layers. The latter type of disorder would involve displacement vectors that are no lattice vectors of the hexagonal sublattice.

Rotational disorder is revealed by $[0001]$ zone ED patterns. The ED pattern of Fig. 10 is a superposition of several ED patterns differing in orientation by rotation about the $[0001]$ zone axis and by mirror reflection in a $\{1230\}$ -type plane (subcell notation), which is mirror plane for the host structure but not for the Eu arrangement. The latter operation gives rise to arrangements of 12 superstructure diffraction spots situated on circles centered on the basic spots and having a radius $|\mathbf{A}_1| = |\mathbf{A}_2|$. Moreover, rotations over arbitrary angles seem to be present as well and complicate the pattern further by double diffraction. The presence of such rotations implies the presence of low-angle twist boundaries on the $[0001]$ planes.

Based on these experimental data, we can propose only a rough structure model. Fine details of the structure that will certainly improve the correspondence between simulated and experimental images are still lacking. The reasonable agreement between experimental and calculated HREM images for several projections though shows that the proposed model is a good approximate.

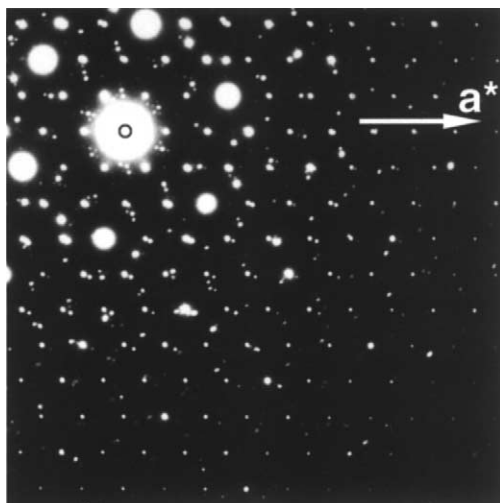


FIG. 10. [0001] zone ED pattern showing orientational disorder in $\text{Eu}_{1.3}\text{Nb}_{1.9}\text{S}_5$ caused by a mirror operation on a $\{12\bar{3}0\}$ -type plane coupled with a rotation about the [0001] zone axis.

DISCUSSION

The proposed structure of $\text{Eu}_{1.3}\text{Nb}_{1.9}\text{S}_5$ can be represented as an alternation of $[\text{Nb}_7\text{S}_{14}]$ slabs with a $[\text{Nb}(\text{Eu}_3\text{S}_4)_2]$ block. Successive $[\text{Nb}_7\text{S}_{14}]$ slabs are oriented in opposite sense with respect to the previous one, resulting in a doubling of the c parameter. The Nb–S distances within the trigonal prisms are 2.45 Å; this distance is typical and found in various polytypes of NbS_2 . Within the mixed (Eu_3S_4) layer the Eu atom is coordinated by four S atoms with interatomic distances of 2.8, 2.9 (twice), and 3.1 Å. The Eu–S distances involving sulfur atoms from the $[\text{Nb}_7\text{S}_{14}]$ slab are about 3.0 and 3.1 Å, while the nearest sulfur atom from the neighboring $[\text{Eu}_3\text{S}_4]^{2-}$ layer is at 3.2 Å. Within the $[\text{Eu}_3\text{S}_4]^{2-}$ layer Eu atoms are reasonably separated from each other by 4.2 Å. Two $[\text{Eu}_3\text{S}_4]^{2-}$ layers are connected through a Nb^{4+} ; its coordination is octahedral, with a Nb–S distance of 2.6 Å, which is acceptable for Nb atoms. Ordering within the $[\text{Eu}_3\text{S}_4]^{2-}$ layer causes the observed $\sqrt{7}a \times \sqrt{7}a$ superstructure, but appears not to have a strong effect on the $[\text{Nb}_7\text{S}_{14}]$ slabs. The interaction between $[\text{Nb}_7\text{S}_{14}]$ and $(\text{Nb}[\text{Eu}_3\text{S}_4]_2)$ slabs is not strong: an ordering in the stacking of $(\text{Nb}[\text{Eu}_3\text{S}_4]_2)$ slabs along the c direction is clearly absent, although the mutual arrangement of neighboring $[\text{Eu}_3\text{S}_4]^{2-}$ layers is well defined. This finding is supported by the presence of curvature defects, observed on $[1\bar{1}00]$ HREM images.

As already mentioned, in the compound $\text{Sr}_6\text{V}_9\text{S}_{22}\text{O}_2$ the octahedral VS_2 slabs are separated by a $[\text{Sr}_6(\text{VOS}_3)_2\text{S}_2]^{4+}$ block (8). The arrangement of this block can be represented as double $(\text{Sr}_3\text{S}_3\text{O})$ layers joined through V^{5+} cations in a tetrahedral coordination and a S_2^{2-} disulfide group. The presence of a disulfide group in $\text{Eu}_{1.3}\text{Nb}_{1.9}\text{S}_5$ is hardly

possible and not in agreement with the observed layer stacking. The absence of oxygen was furthermore also confirmed by EDX analysis.

The $\text{Eu}_{1.3}\text{Nb}_{1.9}\text{S}_5$ compound represents a new structure type of a ternary niobium sulfide, which is quite different from the structures of other NbS_2 derivatives. Among the Eu-containing niobium sulfides several types are known. The structure of $\text{Eu}_{0.167}\text{NbS}_2$ is shown on Fig. 11a. It is considered as an intercalation compound, with Eu^{2+} cations ordered in trigonal-prismatic S interstices between NbS_2 slabs (13). The increase in the Eu-content and the further occupation of regular sites with a prismatic coordination result in strong repulsive interactions; therefore when the Eu content increases another type of structure will become stable. A higher Eu-content is accommodated in the $[(\text{EuS})_{1.5}]_{1.15}\text{NbS}_2$ misfit compound, where Eu and S form the EuS layers with a distorted rock-salt coordination, and triple $(\text{Eu}^{2+}\text{S}-\text{Eu}^{3+}\text{S}-\text{Eu}^{2+}\text{S})$ slabs alternate with NbS_2 sandwiches along the c -axis (Fig. 11c). The presence of Eu in two oxidation states proved by Mossbauer spectroscopy seems to be necessary for the stability of this structure type due to a charge transfer from the $[\text{EuS}]_3$ slab to the NbS_2 slabs (14, 15). The present compound can be considered an intermediate between $\text{Eu}_{0.167}\text{NbS}_2$ and $[(\text{EuS})_{1.5}]_{1.15}\text{NbS}_2$ (Fig. 11c). The oxidation state of Eu in $\text{Eu}_{1.3}\text{Nb}_{1.9}\text{S}_5$ is assumed to be $2+$, consistent with the fact that this compound is isostructural to “ SrNb_2S_5 .” The structure type adapted by ternary compounds in the Eu–Nb–S system apparently depends on the Eu content and its oxidation state.

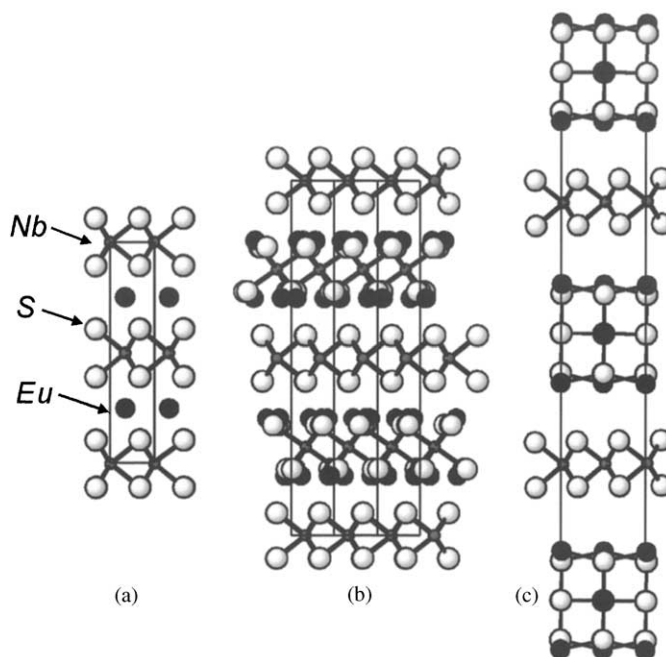


FIG. 11. Comparison of structures for compounds in the Eu–Nb–S system: (a) $\text{Eu}_{0.167}\text{NbS}_2$, (b) $\text{Eu}_{1.3}\text{Nb}_{1.9}\text{S}_5$, (c) $[(\text{EuS})_{1.5}]_{1.15}\text{NbS}_2$.

It will be interesting to compare the structures of $\text{Eu}_{1.3}\text{Nb}_{1.9}\text{S}_5$ with those of other members of the “ ANb_2S_5 ” and “ ATa_2S_5 ” family. From the similarity of the X-ray diffraction patterns we can assume that the accommodation of the A atoms ($A = \text{Sr}, \text{Ba}$) occurs in a similar way: mixed ($A_x\text{S}_y$) layers alternating with NbS_2 sandwiches. The difference in size of the A cations, however, can result in a different arrangement of the ($A_x\text{S}_y$) layer, explaining the variety of observed superstructures.

ACKNOWLEDGMENTS

N.R.K is grateful for financial support of the DWTC during her stay at the University of Antwerp. This work has been partly supported by INTAS-991136, RFBR (00-03-32558), and UIAP-PAI 4/10 grants.

REFERENCES

1. M. S. Whittingham, *Prog. Solid State Chem.* **12**, 41 (1978).
2. S. Kuypers, J. Van Landuyt, and S. Amelinckx, *J. Solid State Chem.* **86**, 212 (1990).
3. M. Saeki, H. Nozaki, and M. Onoda, *Mat. Res. Bull.* **24**, 851 (1989).
4. H. Nozaki, M. Saeki, and M. Onoda, *J. Solid State Chem.* **116**, 392 (1995).
5. M. Saeki, H. Nozaki, and M. Onoda, *Mater. Res. Bull.* **28**, 279 (1993).
6. S. Ya. Istomin, A. Yu. Grippa, O. G. D'yachenko, E. V. Antipov, G. Svensson, and J. L. Tholence, *Physica C* **300**, 67 (1998).
7. G. Van Tendeloo, J. Van Landuyt, and S. Amelinckx, *Phys. Status Solid A* **64**, 105 (1981).
8. J. B. Litter, B.-H. Chen, J. C. Fettinger, B. W. Eichhorn, H. L. Ju, and R. L. Greene, *Inorg. Chem.* **39**, 458 (2000).
9. L. E. Rendon-Diazmiron, C. F. Campana, and H. Stenfink, *J. Solid State Chem.* **47**, 322 (1983).
10. J. Sloan, J. L. Hutchinson, R. Tenne, Y. Feldman, T. Tsirlina, and M. Homyonfer, *J. Solid State Chem.* **144**, 100 (1999).
11. R. De Ridder, G. Van Tendeloo and S. Amelinckx, *Acta Crystallogr. Sect. A* **32**, 216 (1976).
12. D. Van Dyck, R. De Ridder, G. Van Tendeloo, and S. Amelinckx, *Phys. Status Solid A* **43**, 541 (1977).
13. M. Jellinek, *Mater. Res. Bull.* **6**, 169 (1971).
14. L. Cario, A. Lafond, P. Palvadeau, C. Deudon, and A. Meerschaut, *J. Solid State Chem.* **147**, 58 (1999).
15. L. Cario, A. Meerschaut, C. Deudon, and J. Rouxel, *C.R. Acad. Sci. Paris* **1**(IIC), 269 (1998).